Mon. Not. R. Astron. Soc. **318**, 925–937 (2000)

Magnetic and optical spiral arms in the galaxy NGC 6946

P. Frick,[1] R. Beck,[2] A. Shukurov,[3★] D. Sokoloff,[4] M. Ehle[5,6]† and J. Kamphuis[7]

[1]*Institute of Continuous Media Mechanics, Korolyov str. 1, 614061 Perm, Russia*
[2]*Max-Planck-Institut für Radioastronomie, Auf dem Hügel 69, D-53121 Bonn, Germany*
[3]*Department of Mathematics, University of Newcastle, Newcastle NE1 7RU*
[4]*Department of Physics, Moscow University, 119899, Moscow, Russia*
[5]*Max-Planck-Institut für Extraterrestrische Physik, Giessenbachstraße, D-85740 Garching, Germany*
[6]*ESA/XMM SOC, Apartado 50727, 28080 Madrid, Spain*
[7]*Kapteyn Astronomical Institute, Postbus 800, NL-9700 AV Groningen, the Netherlands*

Accepted 2000 June 20. Received 2000 June 20; in original form 1997 September 5

ABSTRACT

The spiral pattern in the nearby spiral galaxy NGC 6946 has been studied using the wavelet transformation technique, applied to galaxy images in polarized and total non-thermal radio emission at $\lambda\lambda 3.5$ and 6.2 cm, in broadband red light, in the $\lambda 21.1$ cm H I line and in the optical Hα line. Well-defined, continuous spiral arms are visible in polarized radio emission and red light, where we can isolate a multi-armed pattern in the range of galactocentric distances 1.5–12 kpc, consisting of four long arms and one short spiral segment. The 'magnetic arms' (visible in polarized radio emission) are localized almost precisely between the optical arms. Each magnetic arm is similar in length and pitch angle to the *preceding* optical arm (in the sense of galactic rotation) and can be regarded as its phase-shifted image. Even details like a bifurcation of an optical arm have their phase-shifted counterparts in the magnetic arms. The average relative amplitude of the optical spiral arms (the stellar density excess over the azimuthal average) grows with galactocentric radius up to 0.3–0.7 at $r \simeq 5$ kpc, decreases by a factor of two at $r = 5$–6 kpc and remains low at 0.2–0.3 in the outer parts of the galaxy. By contrast, the magnetic arms have a constant average relative amplitude (the excess in the regular magnetic field strength over the azimuthal average) of 0.3–0.6 in a wide radial range $r = 1.5$–12 kpc. We briefly discuss implications of our findings for theories of galactic magnetic fields.

Key words: methods: data analysis – galaxies: individual: NGC 6946 – galaxies: ISM – galaxies: kinematics and dynamics – galaxies: magnetic fields – radio continuum: galaxies.

1 INTRODUCTION

Magnetic spiral arms are a new phenomenon in the study of the interstellar medium (ISM) in galaxies. Their existence was first suspected in the galaxies IC 342 (Krause, Hummel & Beck 1989) and M83 (Sukumar & Allen 1989), where regular interstellar magnetic fields were observed to be stronger between the optical spiral arms rather than within them. However, the angular resolution of these observations was insufficient to resolve the arm structure. The most spectacular and convincing case up to date is the galaxy NGC 6946 where polarized radio emission, a tracer of the regular interstellar magnetic field, is concentrated into relatively narrow features located between the material (stellar and gaseous) arms (see Fig. 2). These magnetic features were named '*magnetic arms*' by Beck & Hoernes (1996). The pitch angle of these arms appeared to be the same as that of the adjacent optical arms. Notably, the chaotic magnetic field is generally stronger in the optical arms, as evidenced by the enhancements of unpolarized synchrotron intensity in the optical arms. According to available observations, the regular magnetic field in other well-studied galaxies like M51 and M81 fills almost the whole interarm space without forming distinct magnetic arms (see Beck et al. 1996 and references therein). Less pronounced magnetic arms have recently been detected in NGC 2997, a large southern galaxy which is similar to NGC 6946 (Han et al. 1999).

NGC 6946 is a 'standard' spiral galaxy of Hubble type Sc at a distance of about 5.3 Mpc (Ferguson et al. 1998). In this paper we still use the distance of about 7 Mpc (1 arcmin then corresponds to 2 kpc), to be consistent with our previous papers. The optical spiral structure of NGC 6946 appears multiple-armed and strong,

★ E-mail: anvar.shukurov@newcastle.ac.uk
† Affiliated to the Astrophysics Division, Space Science Department, ESTEC.

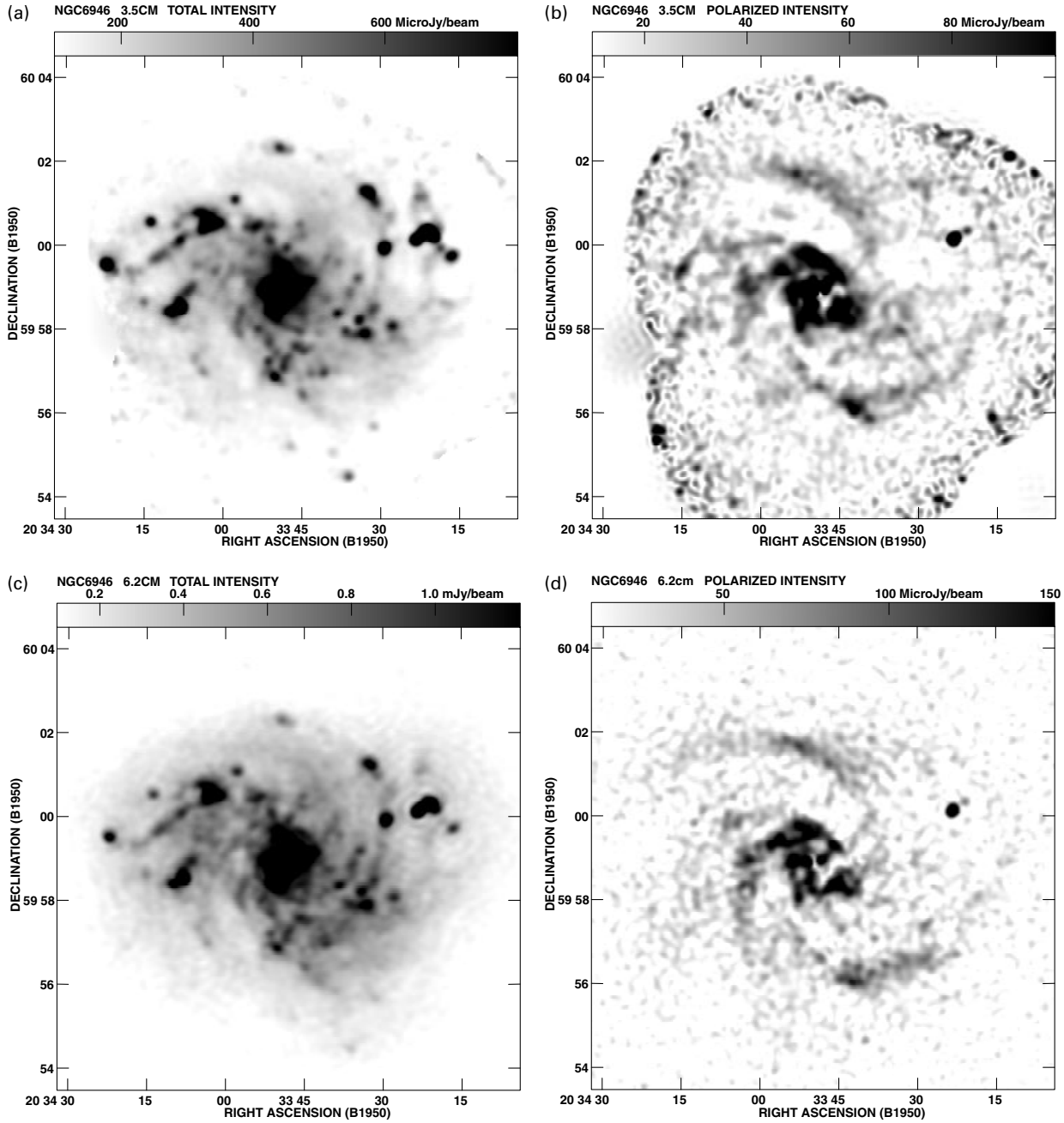

Figure 1. The images of NGC 6946 analysed in this paper (from left to right and from top to bottom): in (a) the total intensity of the radio continuum emission at $\lambda 3.5$ cm, (b) its polarized component, (c) the total intensity of radio continuum emission at $\lambda 6.2$ cm, (d) its polarized component, (e) the broadband red (R) optical intensity, (f) the $\lambda 21.1$ cm radio line emission of H I, and (g) the Hα optical line emission of H II. All the maps have been smoothed to the same angular resolution of 12.5 arcsec, except for the H I map (13×16 arcsec^2 resolution). The grey-scale flux ranges indicated at the top of each panel are in units of mJy/beam (a, c), μJy/beam (b, d), photon kilocounts (e), W.U. (Westerbork Units, 1 W.U. $= 2.2 \times 10^{20}$ H atoms cm^{-2}) (f), and photon counts (g).

albeit irregular in some regions. One spiral arm in the north-east is exceptionally bright. Neutral hydrogen shows very little spiral structure within the optical disc (Kamphuis & Sancisi 1993), while molecular and ionized gas is strongly concentrated in the material arms (Clausset et al. 1991; Ehle & Beck 1993). Ionized gas forms long spiral arms extending out to more than 30 kpc radius (Ferguson et al. 1998).

Ideas on the interaction between magnetic fields and the spiral pattern based on the density wave theory (Roberts & Yuan 1970) considered magnetic fields to be passive and frozen into the interstellar gas. The prediction was that the strongest regular fields should be located at the inner edges of the material arms where the gas density is maximum.

Early galactic dynamo models supposed that the dynamo action is more intense within the spiral arms with the direct consequence of having stronger regular magnetic fields within them (Mestel & Subramanian 1991, Subramanian & Mestel 1993, see also review by Beck et al. 1996). On the other hand, dynamo-generated regular magnetic fields can be stronger in the interarm regions if the dynamo number is larger there, e.g. due to a smaller turbulent

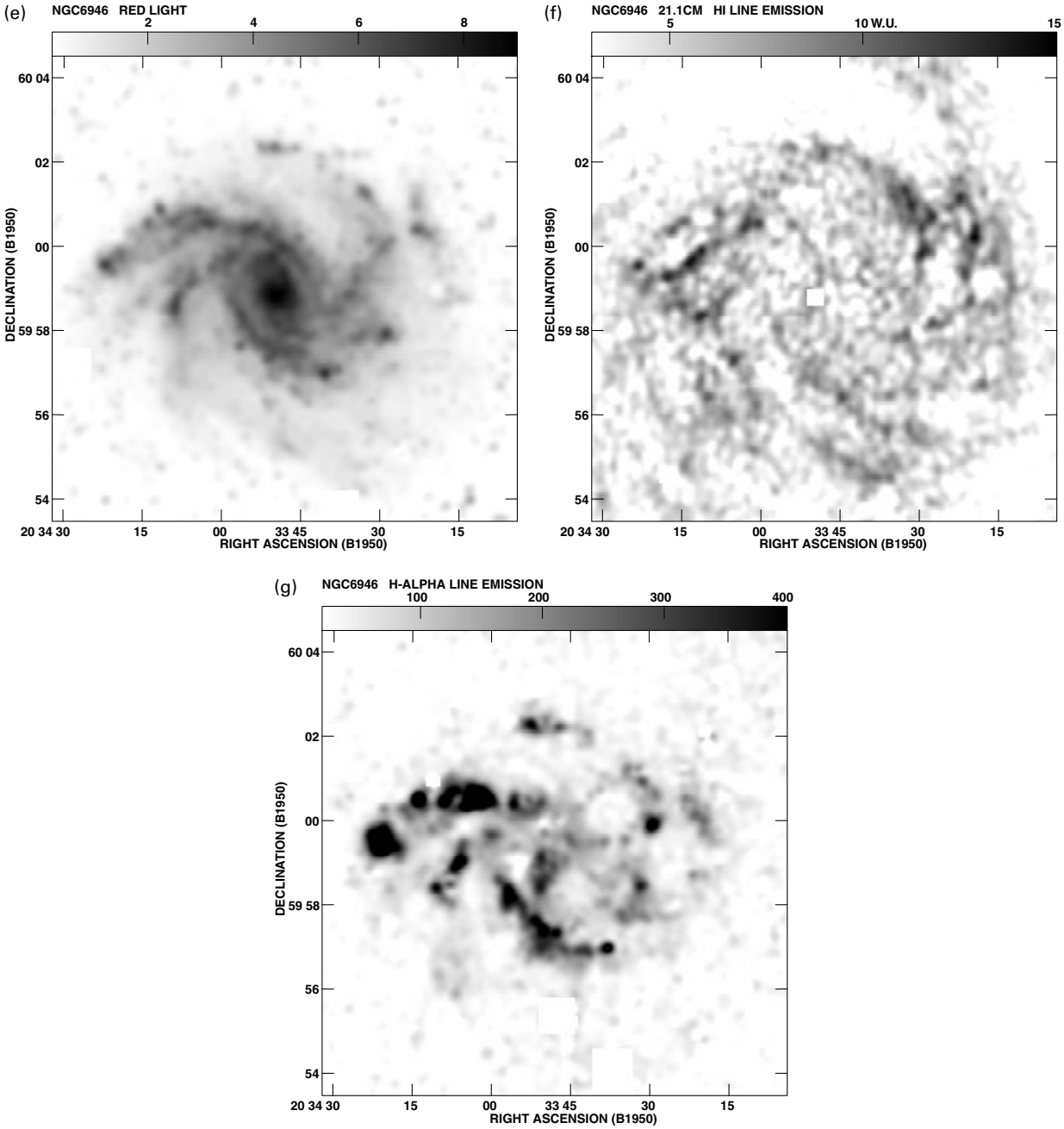

Figure 1 – *continued*

velocity (Shukurov 1998, Shukurov & Sokoloff 1998) or a shorter correlation time (Rohde, Beck & Elstner 1999). As argued by Moss (1998), resonance between the dynamo and the spiral pattern can be vital for magnetic arms. There is yet no unique, convincing explanation of magnetic arms; various possibilities are discussed in Section 5.

In order to clarify the physical relation between material and magnetic arms, one should first obtain quantitative estimates of the positions and widths of the both. Fourier analysis is a well-suited method to detect global patterns which have a nearly perfect azimuthal symmetry and extend over a wide radial range (Schlosser & Musculus 1984; Elmegreen, Elmegreen & Montenegro 1992; Puerari & Dottori 1992). In particular, Elmegreen et al. (1992) have revealed, from blue images of NGC 6946, a dominant two-armed pattern in the inner regions and three arms in the outer parts. Real galactic patterns, however, are neither symmetric nor do they persist at all radii, so that a more general method of analysis is required. Furthermore, Fourier decomposition, when applied to structures with imperfect symmetry, can hardly provide reliable estimates of the amplitudes of the arms and reveal their fine structure – features essential for the subject of this paper.

In this paper we apply wavelets to the spiral pattern recognition (see Section 3 for a discussion of the wavelet techniques). The main advantage of the wavelet transform (in the present context) is the scale-space decomposition of the considered signal: using a suitable analysing wavelet, both the characteristic scale and the position of any localized structure are obtained independently of the general symmetry of the field.

2 OBSERVATIONAL DATA

The total and polarized radio synchrotron intensities trace the total and regular magnetic field strengths, respectively, and the density of cosmic-ray electrons (within a certain energy interval) which originate in supernova remnants. With the diffusion limited by the Alfvén speed ($\simeq 100\,\mathrm{km\,s^{-1}}$ in the hot ISM), cosmic rays can travel over several kiloparsecs distance within their confinement time (a few times 10^7 yr), so that variations in synchrotron intensity at a scale of a few kiloparsecs are mainly due to variations in magnetic field strength.

Optical Hα emission traces the ionized gas heated by bright stars of less than $\simeq 10^7$ yr age while the red light traces much older stars (several times 10^9 yr) and shows the density-wave pattern persisting over this timescale. Emission in the λ21.1-cm line traces neutral atomic hydrogen, but is a worse tracer of spiral patterns as some fraction of the neutral gas is ionized or transformed into molecular gas in the spiral arms. Molecular gas is concentrated in spiral arms and is best observable in the CO lines.

NGC 6946 has been observed in all these spectral ranges. For our study of its spiral patterns we chose the following maps (shown in Fig. 1):

(i) The map of total radio continuum intensity at λ3.5 cm, smoothed to an angular resolution of 12.5 arcsec (Beck, in preparation) (here and below the resolution cited is the FWHM of a Gaussian beam).

(ii) The map of polarized radio synchrotron intensity at λ3.5 cm, smoothed to 12.5 arcsec resolution (Beck, in preparation).

(iii) The map of total radio continuum intensity at λ6.2 cm with an angular resolution of 12.5 arcsec (Beck & Hoernes 1996).

We produced another λ6.2 cm map (not shown in the figures) where all small-scale features (background sources, H II regions and supernova remnant candidates) with a radio flux density of more than 0.5 mJy were subtracted. This limit is the best suitable to remove all sources visible in Fig. 1(c). This map was used only to control our results. The original map turned out to be suitable for our purposes as the wavelet technique efficiently filters out any point sources.

(iv) The map of polarized radio synchrotron intensity at λ6.2 cm with 12.5 arcsec resolution (Beck & Hoernes 1996). This map is also shown as contour lines in Fig. 2.

(v) The map of the optical broadband emission in red light *R* from the digitized Palomar Sky Survey. We subtracted foreground stars from the map and smoothed it to the angular resolution of the radio continuum maps.

(vi) The map of the radio line emission of neutral atomic hydrogen H I at λ21.1 cm, integrated over the whole frequency width of the line (Kamphuis & Sancisi 1993). The H I map has an original resolution of 13×16 arcsec^2 and was not smoothed.

(vii) The map of the optical Hα line emission of ionized hydrogen H II (Ehle & Beck 1993), also shown in Fig. 2. We subtracted foreground stars and smoothed the map to the angular resolution of the radio continuum maps.

The λ3.5-cm maps have been obtained from a combination of radio data from the Effelsberg 100-m telescope operated by the MPIfR and from the VLA operated by the NRAO.[1] The VLA map has been obtained by combining data from three different fields (pointings) because the sensitivity decreases with distance from the field centre (primary beam attenuation). At λ3.5 cm, the width to half power of the primary beam is about 5.4 arcmin. The correction for primary beam attenuation causes the noise to increase with distance from the field centres. The individual maps have been cut at the radius where the noise is 6.6 times larger than that at the field centres. As a result the maps in Figs 1(a) and (b) have sharp edges.

[1] The National Radio Astronomy Observatory is a facility of the National Science Foundation operated under cooperative agreement by Associated Universities, Inc.

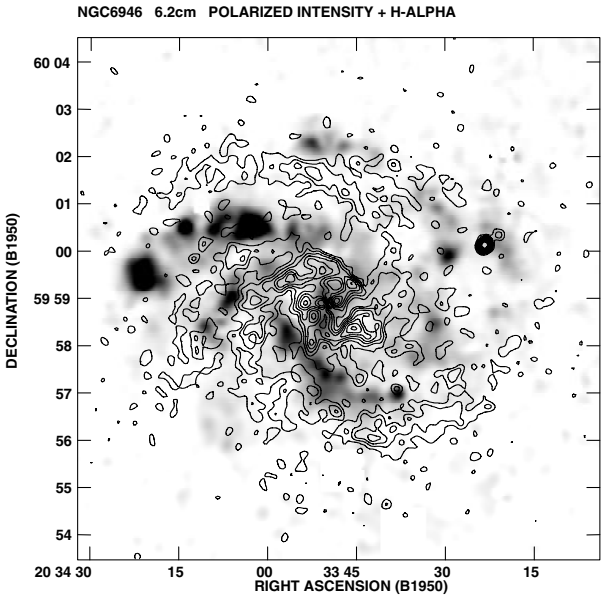

Figure 2. The Hα optical line emission of NGC 6946 in greyscale, as in Fig. 1(g), and contours of polarized radio continuum intensity at λ6.2 cm, as in Fig. 1(d). See Fig. 1 for details. Magnetic arms, visible in polarized emission, are interlaced with those visible in Hα.

The λ6.2-cm maps have also been obtained from a combination of radio data from the Effelsberg telescope and from the VLA. The VLA map has been observed with one single pointing. Primary beam attenuation in the VLA map is much smaller than at λ3.5 cm and has been disregarded in Figs 1(c) and (d).

The *thermal fraction* at λ6.2 cm is 12 per cent (Harnett, Beck & Buczilowski 1989) so that the emission in Fig. 1(c) is mainly of synchrotron origin. At λ3.5 cm the thermal fraction increases to about 17 per cent (using a synchrotron spectral index of −0.85, see Ehle & Beck 1993) so that the synchrotron emission dominates even at this short wavelength. Therefore, our radio maps can be safely used to study magnetic field in the galaxy.

Faraday depolarization DP between λλ3.5 and 6.2 cm is generally small even in the material arms, $0.7 \leq \mathrm{DP} \leq 1$ (Beck, in preparation) where $\mathrm{DP} = p_6/p_3$, and p_6 and p_3 are the fractional polarizations at the two wavelengths. However, DP values decrease to ≃0.5 locally in the inner spiral arms north and west of the centre. At both wavelengths the fractional polarizations in the material arms, $p = 2$–5 per cent are much lower than in the magnetic arms, $p = 20$–45 per cent. Therefore, geometrical (wavelength-independent) depolarization by field tangling on scales smaller than the beam size is much stronger in the material arms than in the interarm regions. Nevertheless, the magnetic arms are difficult to explain by stronger tangling of some regular underlying magnetic field by enhanced turbulence in material arms. In such a case the regular field should fill the interarm space completely which is *not* observed in NGC 6946. The magnetic

arms are also visible as ridges in total intensity (Beck & Hoernes 1996) so that they reveal an *additional* component of the regular field. The fine structure of the magnetic field in the material arms cannot be resolved even with our best resolution of about 8 arcsec, so that the scale of tangling must be smaller than $\simeq$0.3 kpc. Such fields can be regarded as turbulent and are not subject of this paper. In summary, the maps of polarized intensity at both wavelengths are not significantly affected by depolarization and can be used for our analysis of magnetic arms.

We could not consider a map of *molecular gas emission*. The CO map of NGC 6946 by Clausset et al. (1991; see also fig. 1 in Sauty, Gerin & Casoli 1998) does not cover the necessary radial range out to 12-kpc radius. The older map by Tacconi & Young (1989) has insufficient angular resolution and sensitivity.

Broadband optical images of NGC 6946 in *blue light* suffer from strong extinction in the Galactic foreground and thus were also not considered in this study.

The phenomenon of magnetic arms can be seen directly in the images of Fig. 1. We show in Fig. 2 an overlay of two of them, those in Hα and polarized intensity at λ6.2 cm. The spiral pattern seen in Hα is closely related to that in red light (Fig. 1e) and, to a lesser extent, in the total radio emission and H I (Figs 1a, c and f)). The arms seen in polarized radio emission occur almost precisely between those seen in the other tracers. The quantification of this phenomenon is our subject in this paper.

3 PATTERN RECOGNITION USING WAVELETS

To simplify the analysis by making it one-dimensional, we considered the azimuthal variation of a suitable tracer of the spiral structure at various (fixed) radii. Owing to the finite resolution of observations, a certain radial range of galactocentric distances, i.e. a set of rings in the plane of the galaxy should be considered. Furthermore, the data were averaged over sectors in each rings, whose width is determined by the resolution available.

The maps shown in Fig. 1 clearly exhibit a complicated spiral pattern with numerous branches. Most conspicuous are details connected with sharp ridges and it is difficult to isolate with naked eye smooth underlying features which may well be important parts of the galactic structure. One therefore needs an objective tool to isolate and study elements of the galactic spiral structure with allowance for a possibly wide range of their scales and intensities.

A convenient method for such an analysis is the wavelet transformation which is known as an efficient scale-filtering technique (see, e.g. Farge 1992, Holschneider 1995). The wavelet transform of a function $W(x)$ is defined as

$$W_a(x) = \int_{-\infty}^{\infty} W(x')\psi\left(\frac{x'-x}{a}\right) \mathrm{d}x', \qquad (1)$$

where $\psi(s)$, with $s = (x' - x)/a$, is called the analysing wavelet. The latter is required to be a localized function of s with vanishing mean value, $\int_{-\infty}^{\infty} \psi(s)\,\mathrm{d}s = 0$. A particular choice of the analysing wavelet depends on the goals of the analysis. For a study of *scales* present in the signal $W(x)$ (as opposed to a study of the *frequency* content of a quasi-periodic time series), a reasonable choice is a wavelet that provides suitable spatial resolution, known as the *Mexican hat* shown in Fig. 3:

$$\psi(s) = (1 - s^2)\exp\left(-\tfrac{1}{2}s^2\right). \qquad (2)$$

The wavelet transform $W_a(x)$ can be understood as the intensity, at a position x, of that part of the original signal $W(x)$ which has a scale a. For the *Mexican hat*, the scale a is the distance from the centre of the wavelet to its zero point, i.e. $\psi(\pm a) = 0$. Normalization in equation (1) is chosen in such a way that for a signal $W(x)$ containing a structure of a scale A and amplitude B at a position x_0 its wavelet transform is such that $W_A(x_0) = CAB$, where C is a constant of order unity independent of A and x_0. When $W(x)$ is an intensity of emission and x is the azimuthal angle, $r\Delta r W_a(x)$ is proportional to the radiation flux from a structure of an azimuthal scale a located at x, integrated over radius in the ring whose median radius is r and width Δr.

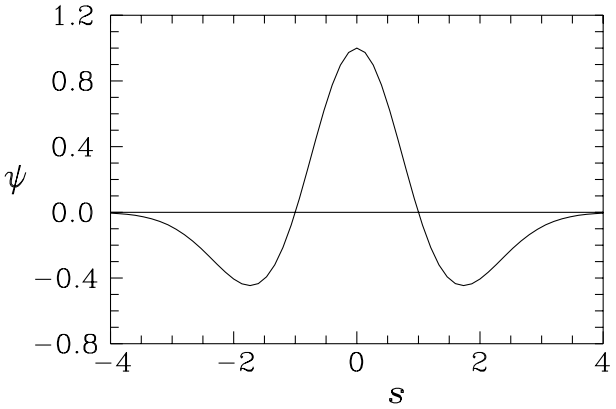

Figure 3. The analysing wavelet, equation (2). The width at half-maximum is about 1.6 times smaller than the separation of the zeros of $\psi(s)$.

The azimuthal distributions of the total intensity of radio emission at λλ3.5 and 6.2 cm and its polarized components, of the λ21.1-cm line emission of the atomic hydrogen gas, and of the broadband red optical light are denoted as $T_3(\phi)$, $T_6(\phi)$, $P_3(\phi)$, $P_6(\phi)$, $H(\phi)$ and $R(\phi)$, respectively. Their wavelet transforms are denoted as $T_{a,3}(\phi)$, $T_{a,6}(\phi)$, $P_{a,3}(\phi)$, $P_{a,6}(\phi)$, $H_a(\phi)$, and $R_a(\phi)$. The data were extrapolated 2π-periodically beyond the range $0 \leq \phi < 2\pi$ in order to perform integration over the infinite domain in equation (1).

The scale a is defined as a characteristic radius of a structure, so that a structure of the scale $a = 90°$ extends over a half of a circle and W_a at $a = 90°$ measures the degree of asymmetry between the two halves of the galaxy in a given ring. This is the largest scale at which it is meaningful to consider the wavelet transform. On the other hand, the size of a sector $\Delta\phi$ introduces the smallest scale equal to $\Delta\phi = 10°$ for $r \leq 4$ kpc and 5° at larger galactocentric radii.

Wavelet analysis can be considered as a generalization of Fourier analysis. A well-known property of Fourier analysis is that it provides accurate estimates of the period of a nearly *periodic* structure, but it is less successful with isolated, non-periodic (and even quasi-periodic) structures. Elmegreen et al. (1992) analysed images of 18 galaxies in order to reveal two- and three-arm symmetries by superposing the original image and its copies rotated by 180° and $2 \times 120°$, respectively. Puerari & Dottori (1992) note that Fourier analysis does not yield any clear result for NGC 6946. As there is no universal approximation for spiral arms in real galaxies (say, in the form of logarithmic spirals), a two-dimensional Fourier analysis can hardly lead to any clear results (Kennicutt 1981).

Wavelet analysis is devised to resolve similar difficulties. Unlike harmonic functions, wavelets are localized in space – see equation (2) and Fig. 3. Therefore, the wavelet transform $W_a(\phi)$

explicitly preserves information on both the scale of a structure and its position in physical space and thereby contains two parameters, a and x.

One could apply a two-dimensional wavelet transform to the galaxy images, in particular anisotropic wavelets having the shape of spiral segments. However, we restrained ourselves from such an analysis not only because it involves an unnecessarily large number of free parameters, but also because it is restricted to a certain model of the spiral arms, e.g. the logarithmic-spiral or any other approximation (see, however, Section 4.6). Thus, we used a one-dimensional wavelet transform applied to the data at a given galactocentric radius. This allowed us to follow the angular shift of a given structure with radius and thereby to isolate spiral arms and to determine their pitch angles.

4 RESULTS

4.1 The spiral patterns derived from wavelet transforms

We illustrate typical features of the wavelet transforms $P_{a,6}(\phi)$ and $R_a(\phi)$ for NGC 6946 in Fig. 4 where results for the four rings between $r = 4.0$ and 6.0 kpc are shown in the (ϕ, a)-plane. The maxima of the wavelet transform $W_a(\phi)$ in the (ϕ, a)-plane, which are surrounded by closed level lines correspond to structures that have a definite azimuthal scale. The localization of such a maximum in the (ϕ, a)-plane gives the position of the centre of the corresponding feature along the ϕ-axis and its scale a. Minima of the signal result in negative extrema of $W_a(\phi)$ located between the positive maxima.

We disregarded the λ3.5-cm data in those parts of the outer rings where the noise in synchrotron emission, corrected for the primary beam attenuation, was larger than three times the central value. For other tracers in the radio range, no correction for the primary beam attenuation is needed because of larger primary beams. We have applied our analysis to those galactocentric distances where spiral arms are clearly visible; generally, this is true within about 12 kpc from the centre. We neglected the maxima that have unphysically large scales ($a > 90°$) or are too weak ($W_a < 0.03 \max W_a$ in each ring).

The R_a map has also a different type of structures represented by a system of level lines which are not closed but converge, for $a \to 0$, to some value of ϕ. These structures correspond to sharp, unresolved peaks (ridges) that cannot be characterized by any well-defined scale. They arise only in the optical map because the resolution of the optical data is significantly higher than the size of our sectors. These structures are also included into our analysis.

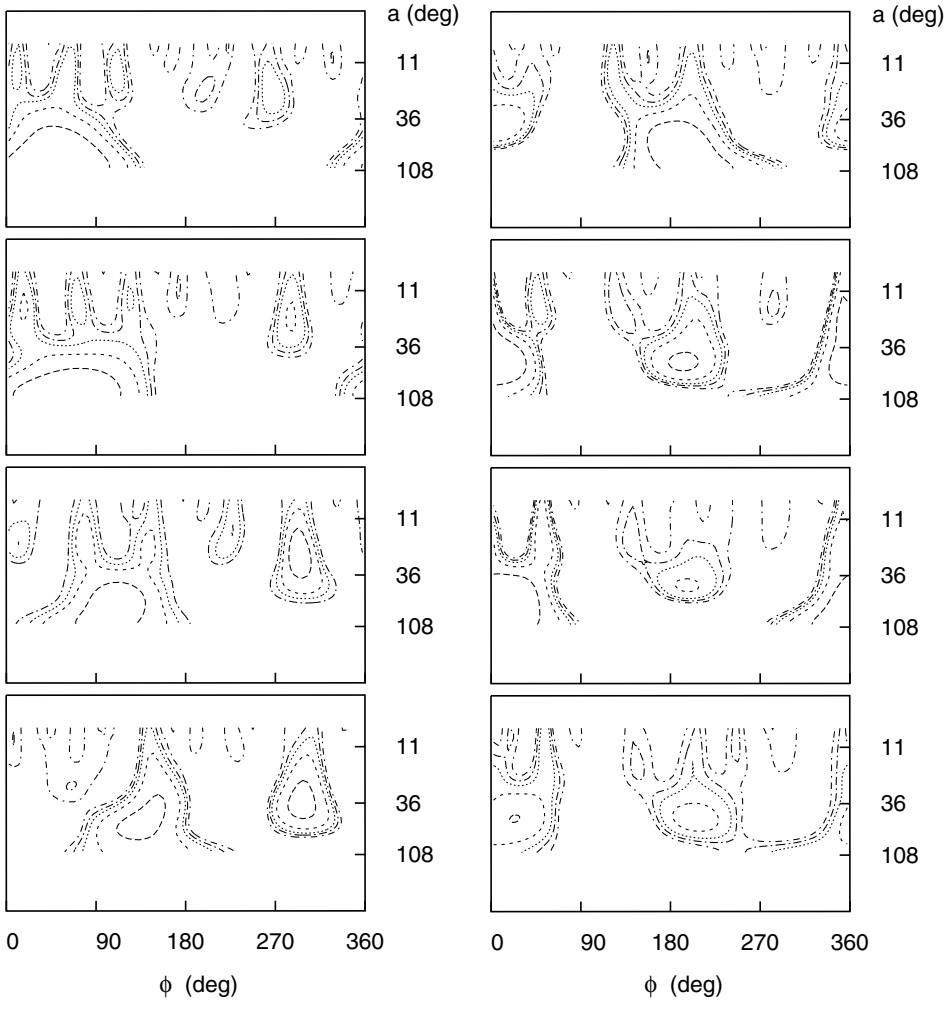

Figure 4. Level lines of the wavelet transforms in the (ϕ, a)-plane (only for positive values of W_a) for the polarized radio intensity at λ6.2 cm, $P_{a,6}$ (the left-hand panel), and the broadband red optical light, R_a (the right-hand panel), in the rings of 0.5-kpc width between $r = 4.0$ (top) and 6.0 kpc (bottom) in the plane of NGC 6946. The contour separation is a factor of 2.

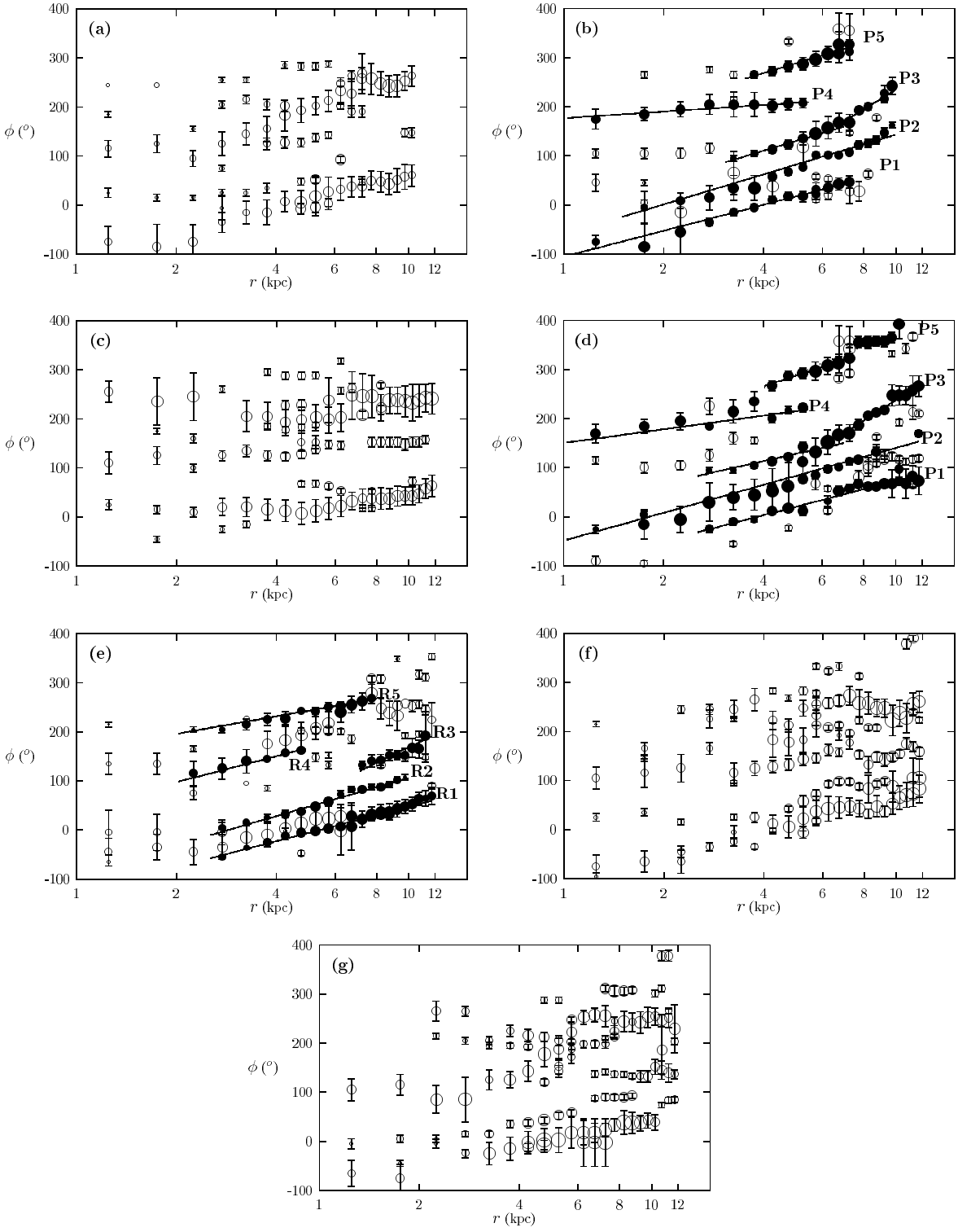

Figure 5. Positions of the wavelet maxima in (a) the total radio intensity at $\lambda 3.5$ cm, (b) the polarized radio intensity at $\lambda 3.5$ cm, (c) the total radio intensity at $\lambda 6.2$ cm, (d) the polarized radio intensity at $\lambda 6.2$ cm, (e) the broadband red optical intensity, (f) the radio line emission of neutral atomic hydrogen, and (g) the optical line emission of ionized hydrogen maps of NGC 6946 in the $(\log r, \phi)$-plane (inclined by $\simeq$30° to the sky plane). r is measured in kpc and ϕ in degrees; ϕ runs counter-clockwise from the north-eastern major axis of NGC 6946 (position angle PA $\approx$ 52° with respect to the northern direction). Bars indicate the azimuthal scale of the structure. All points are plotted at the median radius of the corresponding ring. The size of the symbols is proportional to the magnitude of the wavelet transfer. Filled symbols indicate the maxima included into the spiral arms discussed in the text. Segments of straight lines indicate logarithmic fits (see Table 1) as discussed in the text.

We show in Fig. 4 examples for the level lines of the wavelet transform; to simplify the appearance of the figure only contours corresponding to its positive values are shown. One can clearly see two broad maxima in both red light and polarized intensity. The central position of a maximum shifts in azimuthal angle from one ring to the next, as expected for a spiral.

All results for the 22 rings of 0.5-kpc width in the galactocentric radius range $1 \leq r \leq 12$ kpc are summarized in Fig. 5 where we show the positions of the maxima in the (r, ϕ)-plane for all the tracers. For each maximum, we indicate its scale as a bar whose total length is equal to $2a$. It should be emphasized that *the bars indicate the azimuthal extent of a structure, but not the error of its position.* On the other hand, the accuracy of the position of a structure is related to its scale, so that the bars of Fig. 5 also provide a crude indication of the accuracy of the spiral arm positions.

A discrete source is prominent in both polarized maps and in the red light, located at $r \simeq 7$–9 kpc, $\phi = 230°$–$260°$ in the $\lambda 3.5$-cm polarized emission map. We do not show the corresponding maxima in Fig. 5.

We applied a similar analysis to the map of total intensity at $\lambda 6.2$ cm where most unresolved sources had been removed (see Section 2). The result is not much different in spite of very strong differences in the level of the wavelet coefficients: a significant decrease in T_a when the sources have been subtracted indicates that the sources cluster in those regions where the diffuse total radio emission is enhanced. Wavelet transforms at the scales of interest are not contaminated by such small-scale structures

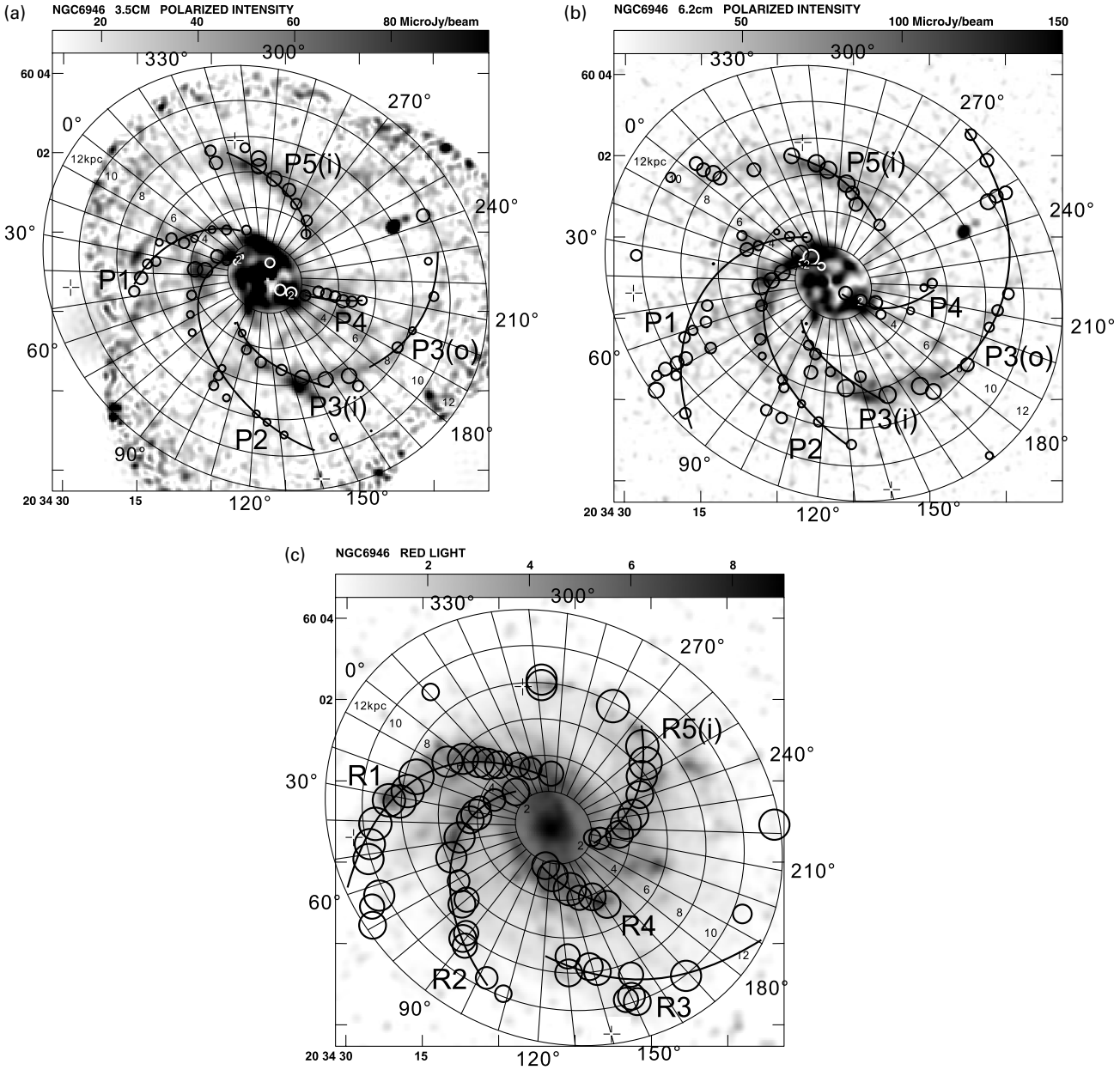

Figure 6. The backbones of spiral arms in polarized radio intensity at $\lambda 3.5$ cm (a), $\lambda 6.2$ cm (b) and in red optical light (c), superimposed on the corresponding grey-scale maps and the polar coordinate grid. Galactocentric radii in kiloparsecs are indicated along the major axis and the polar angle is given at the edge of the grid. The wavelet maxima of Fig. 5 are shown with circles of a size proportional to $\ln rW_a$, and the logarithmic–spiral fits of Table 1 are shown with solid lines. The coordinates on the sky are as in Fig. 1.

because of the wide scale separation and of the good scale resolution of the wavelet.

The width of a structure, $2a$, is the separation of those positions where the signal becomes as weak as the average level in a given ring. For the *Mexican hat* wavelet, $2a$ is about 1.6 times larger than the width at half maximum usually quoted in the literature (see Fig. 3).

In *total radio intensity* (Figs 5a and c) the positions of the maxima show a moderate correlation with those in red light, but there is a tendency for the maxima to be arranged at a constant azimuth which reflects the elongated shape of the isophotes in the galaxy plane. Inspection of Figs 1(a) and (c) confirms that the total radio emission is more extended along the azimuthal angles $\phi \simeq 20°$ and 240°, following the distribution of the H I gas in the outer regions (Kamphuis & Sancisi 1993). Comparison of Figs 5(a), (c) and (f) makes it clear that the total intensity and H I distributions are correlated at large scales. However, the total intensity is possibly even better correlated with the total gas density (neutral and molecular), as observed in M31 (Berkhuijsen, Bajaja & Beck 1993). Spiral-shaped features in Figs 1(a) and (c) apparently follow the spiral structure seen in the optical image (e), but they are not pronounced well enough to dominate the distribution of the total synchrotron intensity.

The spiral structures traced by emissions of *neutral atomic hydrogen* and of *ionized hydrogen* (Figs 5f and g, respectively) are less ordered than in red light (Fig. 5e). Some arms visible in red light can be traced in both H I and Hα, and some features of the H I distribution correlate with the polarized emission. A sequence of points that occur at an almost constant azimuthal angle in Figs 5(f) and (g) result not from spirals but rather from elongated isophotes.

4.2 Magnetic and optical spiral arms

Figs 5 (b), (d) and (e) allow us to identify well-defined, long spiral arms in *polarized intensity* and *red light*. We adopt the following nomenclature, illustrated in Figs 5 and 6 and used in Table 1. The arms visible in polarized radio emission are called P1, P2, P3, P4 and P5, with P1 starting at $r = 1.25$ kpc, $\phi = 285°$, the next one being adjacent towards larger values of ϕ (i.e. the next in the counter-clockwise direction). The structures P1, P2 and P5 are long spiral arms. Arm P3 apparently bifurcates from P2 at about 4-kpc radius. At 10-kpc radius, Arms P1, P2, P3 and P5 form an asymmetric spiral pattern, with three arms in the southern half (P1, P2 and P3) but only one arm (P5) in the northern half. The short spiral segment P4, as seen at λ3.5 cm, extends with a mild pitch angle from $r = 1.25$ kpc, $\phi = 175°$, becomes almost radial at $r = 2.75$ kpc, $\phi = 205°$ and disappears at $r = 5.25$ kpc, $\phi = 208°$.

The data at λ3.5 cm are generally reliable within $r \simeq 10$ kpc, but only out to $r \simeq 8$ kpc in the eastern part of the galaxy (in the region of P1 and P5) due to the positions of the three fields chosen for the VLA observations. The radial extent of the structures at λ3.5 cm in the outer galaxy, given in Table 1, reflects this observational restriction.

The above positions are for the polarized arms at λ3.5 cm. At λ6.2 cm, the picture is generally the same, but the arms can be traced to larger radii. For example, Arm P5 is detected by wavelet analysis out to $r \approx 7.5$ kpc at λ3.5 cm, and further to 10.5 kpc at λ6.2 cm.

For the red light, we similarly introduce R1, R2, R3, R4 and R5, with R1 starting at $r = 2.75$ kpc, $\phi = 305°$. Arm R3, clearly visible in the outer regions at $r > 7.25$ kpc, $\phi > 133°$, apparently bifurcates from arm R2 at a smaller radius $r \simeq 4$ kpc, similarly to the polarized arms P3 and P2. Arm R4 can be seen only in the inner galaxy. Arm R5 is well visible in Fig. 1(e) in the north out to 9.5 kpc, but its pitch angle varies with radius rather strongly and becomes small at $r \gtrsim 8$ kpc, so that its azimuthal scale becomes very large and our analysis fails to detect it in all the rings. Similarly to the corresponding polarized structures, Arms R1, R2 and R3 are located in the eastern and southern parts of the galaxy, with only R5 in the north.

The imperfect symmetry of the spiral pattern makes Fourier analysis less suited to the description of the spiral structure in NGC 6946. Being biased towards perfectly symmetric patterns, it has isolated a two-armed pattern in the inner galaxy having combined Arms R1 and R2 and Arms R4 and R5, and a three-armed pattern in the outer regions comprising the arms R1, R3 and R5 (Elmegreen et al. 1992, plate 16). Arm R3 could be detected by Elmegreen et al. only when the two-arm component had been subtracted from the optical image. The finer structure of the galactic spiral pattern revealed by the wavelet analysis has obvious physical significance as it can be seen in both optical and radio ranges.

Detailed parameters of the structures in polarized emission and in red light obtained by logarithmic spiral fitting as discussed in Section 4.3 are given in Table 1. The plots in Fig. 5 are in log–linear scale, so a logarithmic spiral would trace a straight line.

Most features detected in polarized emission and red light can also be found a posteriori in the neutral and ionized gas distributions (Figs 5f and g), but they are less clear and less structured. Our analysis shows that spiral arms are best visible in the light of relatively old stars (Elmegreen & Elmegreen 1984) and in the large-scale regular magnetic field. The ionized gas and the total (mostly turbulent) magnetic field mark the sites of recent

Table 1. Spiral arms in NGC 6946.

Name	r (kpc)	ϕ_5 (°)	ϕ_{10} (°)	p (°)
Regular magnetic field, λ3.5 cm (polarized radio intensity)				
P1	1.0–7.5	18 ± 23	70 ± 23	37 ± 9
P2	1.5–10.0	83 ± 15	143 ± 15	33 ± 6
P3 inner	3.0–7.0	130 ± 23	–	33 ± 7
P3 outer	7.0–10.0	–	234 ± 23	18 ± 12
P4	1.0–5.5	208 ± 37	–	71 ± 28
P5 inner	3.5–7.5	288 ± 28	–	33 ± 11
Regular magnetic field, λ6.2 cm (polarized radio intensity)				
P1	2.5–12.0	21 ± 19	73 ± 19	37 ± 10
P2	1.0–12.0	82 ± 19	140 ± 19	35 ± 7
P3 inner	2.5–7.0	128 ± 19	–	41 ± 8
P3 outer	7.0–12.0	–	237 ± 27	17 ± 14
P4	1.0–5.5	215 ± 21	–	55 ± 13
P5 inner	4.0–7.5	287 ± 33	–	31 ± 13
Red optical light				
R1	2.5–12.0	354 ± 8	45 ± 8	38 ± 4
R2	2.5–10.0	47 ± 11	106 ± 11	34 ± 5
R3 outer	7.0–12.0	–	168 ± 19	22 ± 15
R4	2.0–5.0	167 ± 9	–	38 ± 4
R5 inner	2.0–8.0	243 ± 11	–	48 ± 9

Notation: r is the range of galactocentric radii in which the arm is discernible, ϕ_5 and ϕ_{10} are the azimuthal positions of the logarithmic fits to the arms at radii of 5 kpc and 10 kpc, respectively, and p is the pitch angle averaged over the above radial range. The names of the arms and the fits are indicated in Fig. 6. The errors given are the 2σ values.

star formation. The neutral atomic gas forms distinguishable spiral arms only in the outer regions of NGC 6946 where star formation is low (Boulanger & Viallefond 1992; Kamphuis & Sancisi 1993). In the region $r \leq 12$ kpc H I shows an irregular and chaotic pattern, plausibly controlled by star-formation activity. The spiral arms are well visible in the molecular CO line emission (Clausset et al. 1991), but a complete CO map of NGC 6946 out to 12 kpc radius is still lacking.

4.3 Pitch angles of the magnetic and optical arms

The arms can well be approximated by logarithmic spirals over a wide radial range. To estimate the pitch angle we fitted the dependence $(\tan p)^{-1} \ln r/r_{10} - (\phi - \phi_{10}) = 0$ to the positions of the maxima of the wavelet transforms in the (r, ϕ)-plane (Fig. 5). Arms 3 and 5 cannot be fitted with a single logarithmic spiral because their pitch angles decrease significantly with increasing radius. For Arm 3 we defined two radial ranges for which separate fits are given in Table 1. For Arm 5, visible out to $r = 9.5$ kpc, $\phi = 350°$ in red light and $r = 10.5$ kpc, $\phi = 40°$ at $\lambda 6.2$ cm, the fits for the outer part yield highly uncertain values because it runs almost azimuthally (at a small pitch angle).

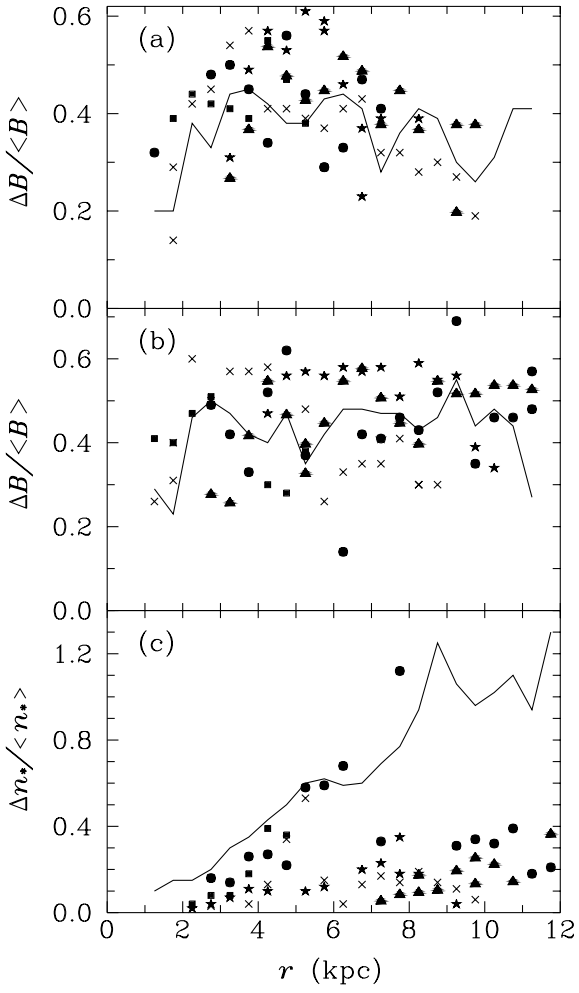

Figure 7. The ratio of the excess of the regular magnetic field in the arms to the azimuthal average as obtained from wavelet transforms of the polarized intensity, equation (3), at $\lambda 3.5$ cm (a) and $\lambda 6.2$ cm (b) and a similar measure of the amplitude of the spiral arms in the stellar number density visible in the red light (c), Equation (4). Circles: Arms 1, crosses: Arms 2, triangles: Arms 3, squares: Arms 4, and stars: Arms 5. Two points belonging to the stellar Arm 1 have been omitted in panel (c): $\Delta n_*/\langle n_* \rangle \approx 1.6$ and 2.0 at $r = 8.25$ and 8.75 kpc, respectively. Solid lines show these quantities as determined from the azimuthal averages of the emission intensities, equations (5) and (6).

The weighted least-squares fits (with weights equal to the scale shown with bars in Fig. 5) yield the pitch angles and phases given in Table 1 and shown in Fig. 6. The errors are 2σ values obtained from the χ^2 criterion. With the weights chosen, the residual was always much smaller than the corresponding value of χ^2, so the errors are overestimated.

The average pitch angles of all respective arms well agree with each other, and this agreement is good enough to be meaningful even with the overestimated errors. The only exception is Arm 4. The average pitch angles for Arms 1, 2 and the inner part of Arm 5 are about 35° for both the magnetic and the optical arms differing by just a few degrees, in spite of their different locations in azimuth. The outer part of Arm 3, a plausible result of bifurcation from Arm 2, has a significantly smaller pitch angle ($\simeq 20°$) in all three tracers. On the other hand, the short Arm 4 has a larger pitch angle than most other features. The inner part of Arm 5 has a somewhat larger pitch angle in red light than in polarized emission.

4.4 Phase shifts between the magnetic and optical arms

There is a remarkably detailed connection between the positions of polarized and material arms traced by the red light: polarized structures are interlaced with the red arms.

The fact that the two most prominent polarized and optical arms (R2/3 and P2/3, and R5 and P5) are interlaced was already noted by Beck & Hoernes (1996) from qualitative analysis of their $\lambda 6.2$-cm map. The wavelet analysis performed here has identified confidently *five* extended structures in each tracer. Their positions and pitch angles have been determined and it has been revealed that they are interlaced even in very fine details.

The similarity in pitch angles between magnetic arms and the *preceding* (with respect to the galactic rotation) optical arms gives strong evidence that the magnetic arms are *phase-shifted images* of the material arms which is a clue to understand their origin (Section 5). This azimuthal phase shift can be followed down to detailed structures like the bifurcation of Arm 2 at $r \simeq 4$ kpc which occurs at $\phi \simeq 30°$ in red light and at $\phi \simeq 65°$ in polarized emission.

The average azimuthal phase shifts between the polarized and optical arms can be derived from Table 1. At $r = 5$ kpc the phase shifts are $\Delta\phi_5 = 26 \pm 12°$, $36 \pm 11°$ and $45 \pm 17°$ for Arms 1, 2 and 5, respectively. For the outer part of Arm 3, $\Delta\phi_{10} = 68 \pm 17°$. Here the phase of a magnetic arm was taken as the arithmetic mean value of the phases of the polarized arms seen at $\lambda\lambda 3.5$ and 6.2 cm, and the error was adopted as the maximum error between the two wavelengths (we note that the median values of ϕ_5 and ϕ_{10} at $\lambda\lambda 3.5$ and 6.2 cm are very close to each other). The errors quoted for $\Delta\phi$ are 1σ values.

Although the above values of $\Delta\phi_5$ and $\Delta\phi_{10}$ formally agree with each other within errors, the difference can be significant because the errors are overestimated (Section 4.3). Still it is clear that all four magnetic arms are located almost precisely between the optical arms, forming an *interlaced spiral structure*. The phase shift varies with radius only weakly (a consequence of the approximately logarithmic-spiral shape of the arms), and this contradicts the hypothesis that magnetic arms arise because of a

delayed response of magnetic field, with a constant delay time, to a perturbation produced in the material arms (see Section 5).

4.5 Arm amplitudes

The values of the wavelet transform can be used to quantify the amplitudes of the arms seen in different tracers. Consider the polarized radio intensity P. It is proportional to a weighted value of $B_{\rm reg}^2 n_{\rm e}$ (we neglect a small inclination of $\boldsymbol{B}_{\rm reg}$ to the sky plane), where $B_{\rm reg}$ is the regular magnetic field strength and $n_{\rm e}$ is the number density of cosmic ray electrons, proportional to the total energy density of cosmic rays. Under energy equipartition or pressure balance between cosmic rays and magnetic field, we have $n_{\rm e} \propto (B_{\rm reg}^2 + b^2)$, where b is the rms turbulent magnetic field. Since in spiral galaxies b usually exceeds $B_{\rm reg}$ by a factor of at least 2, we obtain $P \propto B_{\rm reg}^2 b^2 (1 + B_{\rm reg}^2/b^2) \approx B_{\rm reg}^2 b^2$ for $b \gg B_{\rm reg}$. Thus, the polarized intensity of synchrotron emission is roughly proportional to the regular magnetic field squared, irrespective of whether or not a balance with cosmic rays is maintained, provided only that $b \gg B_{\rm reg}$. Assuming that the energy density of the turbulent magnetic field b varies only weakly with ϕ (as indicated by the weak azimuthal variation in the total radio intensity – see Fig. 1; cf. Shukurov 1998), we can adopt $P_a \propto a B_{{\rm reg},a}^2$ if b does not scale with $B_{\rm reg}$ and $b \gg B_{\rm reg}$, where $B_{{\rm reg},a}$ is the regular field component having the azimuthal scale a.

The degree of polarization observed locally within the magnetic arms can be as high as 30 per cent (Beck & Hoernes 1996) indicating that $B_{\rm reg}$ is, locally, of similar strength as b or even stronger if the limited resolution is taken into account. On the large scales of our analysis, however, the degree of polarization is lower (8 per cent on average over the galaxy), and our approximation remains valid.

We did not introduce any correction for depolarization that can be stronger in the material arms than in the interarm space because the maps of polarized intensity at $\lambda\lambda 3.5$ and 6.2 cm are not significantly affected by Faraday depolarization (see Section 2).

Wavelet transform is insensitive to any mean value of the signal, so P_a/a is the excess of the polarized intensity in the structure of a scale a above the average value. Then the ratio of the excess in the regular magnetic field strength in the arm of a scale a, $\Delta B_{\rm reg}$ (called the arm amplitude hereafter), to the azimuthally averaged strength, $\langle B_{\rm reg}\rangle$, is given by

$$\frac{\Delta B_{\rm reg}}{\langle B_{\rm reg}\rangle} = \left(\frac{k P_a}{a\langle P\rangle}\right)^{1/2}, \tag{3}$$

where we assume that $P_a = k a B_{{\rm reg},a}^2$, k is a normalization factor calculated below and angular brackets denote azimuthal averaging. We show in Figs 7(a) and (b) the resulting relative amplitude of the regular magnetic field in the magnetic arms for each ring as a function of radius as obtained from the polarized intensity at $\lambda\lambda 3.5$ and 6.2 cm.

Since the intensity of the red light R is proportional to the stellar surface density $n*$, the enhancement in the stellar surface density produced by the structure of a scale a can be estimated as

$$\frac{\Delta n*}{\langle n*\rangle} = \frac{k R_a}{a\langle R\rangle}. \tag{4}$$

This quantity is shown in Fig. 7(c) as a function of radius for individual spiral arms (where we have omitted, for representation purposes, two points with $\Delta n*/\langle n*\rangle \approx 1.6$ and 2.0 at $r = 8.25$ and 8.75 kpc, respectively; both points belong to Arm 1).

To confirm independently the estimates of the arm amplitudes obtained from wavelet transforms, we also used the following procedure. Assuming that the variation of $B_{\rm reg}$ with azimuth is sinusoidal, $B_{\rm reg} = \langle B_{\rm reg}\rangle + \Delta B_{\rm reg} \sin m\phi$, and $B_{\rm reg} \propto P^{1/2}$, the ratio $\Delta B_{\rm reg}/\langle B_{\rm reg}\rangle$ can be obtained as

$$\left\langle \frac{\Delta B_{\rm reg}}{\langle B_{\rm reg}\rangle} \right\rangle = \sqrt{2\left(\frac{\langle P\rangle}{\langle P^{1/2}\rangle^2} - 1\right)}. \tag{5}$$

The azimuthal averages are independent of the value of m.

In a similar manner, the azimuthally averaged measure of the arm amplitude in terms of the stellar surface density is provided by

$$\left\langle \frac{\Delta n*}{\langle n*\rangle} \right\rangle = \sqrt{2\left(\frac{\langle R^2\rangle}{\langle R\rangle^2} - 1\right)}. \tag{6}$$

The azimuthally averaged relative amplitudes of the arms are shown as solid lines in Fig. 7.

The wavelet transforms have been normalized to ensure that equations (3) and (4) yield the same results as equations (5) and (6), respectively, for a sinusoidal signal. The normalization factors are $k = 1.28$ for P_a and $k = 1.64$ for R_a, respectively.

Despite a scatter of the points in Fig. 7, there are clear radial trends. The arm contrast in magnetic field, $\Delta B_{\rm reg}/\langle B_{\rm reg}\rangle$ is more or less constant along the radius and its typical value is 0.3–0.6. On the contrary, $\Delta n*/\langle n*\rangle$ systematically grows with radius at $r \lesssim$ 5–6 kpc reaching 0.3–0.7, then abruptly decreases by a factor of about two and remains at a low level of 0.2–0.3 in the outer parts of the galaxy. This behaviour is pronounced especially well in the longest Arms R1 and R2, but not in R5 (Arm R4 is visible only in the inner galaxy where it follows the trend). It is notable that the change in the arm properties occurs near the corotation radius $r \simeq 5$ kpc (Elmegreen et al. 1992). Incidentally, Arm 4 extends out to this radius. It is also interesting that the relative intensities of magnetic and optical arms depend distinctly on galactocentric radius.

Another notable feature of the optical Arm R1 is that it contains substructure whose relative amplitude continues to grow with radius out to about 9 kpc (two points not shown in Fig. 7c – see the figure caption). The azimuthally averaged arm contrast shows a similar sharp peak at that radius.

As indicated by the difference between wavelet amplitudes and the azimuthally averaged arm contrast, the azimuthal variation of $\Delta n*$ strongly deviates from a simple sinusoidal law at $r \gtrsim 5$ kpc. This can make misleading the Fourier analysis of the optical spiral pattern. The relation between $\Delta n*/\langle n*\rangle$ obtained from the wavelet transform and from the azimuthal averages indicates that the stellar arms are wider than the interarm regions, with an 'interarm' region defined as that where $n* < \langle n*\rangle$.

If $B_{\rm reg}$ and b depend similarly on the averaged parameters of the interstellar medium, the ratio $B_{\rm reg}/b$ will only weakly vary with position. If $B_{\rm reg}/b = {\rm const}$, we obtain $P \propto (B_{\rm reg}^2 + b^2) B_{\rm reg}^2 \simeq B_{\rm reg}^4$. With this scaling, the azimuthal averages would be half of those for $P \propto B_{\rm reg}^2$, whereas the estimates from the wavelet transforms would be equal to the square root of the values given in Fig. 7.

The azimuthally averaged quantities are a poorer measure of the arm amplitude than the estimates derived for each arm individually from the wavelet transforms, in particular because the former assume that the widths of the arms and interarm regions are equal to each other and that all the arms are of equal amplitudes.

Thus, the amplitudes of the magnetic arms vary with radius rather differently from the arms traced by the old stellar population: the former are more or less equally well pronounced at all radii between about 1 and 11 kpc, whereas the relative amplitudes of the stellar arms systematically grow with radius at $r \lesssim 5$ kpc and experience significant decrease near the corotation radius. This behaviour may help to understand the nature of the magnetic arms in future studies.

4.6 Arm widths

The angular scales of the structures, related to the arm widths, are shown in Fig. 5 as bars. The scales often show significant variation from one ring to another. Apart from genuine variation in the arm width, the width measured along azimuth is sensitive to local variations in the arm's pitch angle. Since we can only introduce a global pitch angle from our logarithmic spiral fits (see Table 1), these local geometric variations cannot be rectified. In order to obtain meaningful estimates of the arm widths one might use anisotropic wavelets, but we restrain ourselves from this complication in this work.

5 DISCUSSION

We have found evidence that the structures detected in polarized radio intensity and red light are physically related to each other. The polarized arms are located almost precisely midway between the adjacent material arms, with fairly constant azimuthal phase shifts resulting from similar values of the arm pitch angles.

The magnetic arms cannot be a superficial result of a stronger Faraday depolarization in the material arms because they appear very similar at two different, rather short radio wavelengths (Figs 1b and d). The magnetic arms can hardly be explained by stronger field tangling by enhanced turbulence in the material arms (see Section 2).

Apart from R3 and P2, the material and polarized arms do not intersect. Furthermore, the phase shift between them does not vary strongly with radius. This makes implausible the idea that the shift of the magnetic arms with respect to the optical ones is due to a (constant) time delay τ in the response of magnetic field generation mechanism (e.g. a dynamo) to the perturbation from the spiral arms. If this were the case, then the phase shift $\Delta\phi$ would be a function of radius, $\Delta\phi = \tau[\Omega(r) - \Omega_{\rm p}]$, where $\Omega(r)$ is the angular velocity of the gas and $\Omega_{\rm p}$ is that of the material arms. In addition, the material and polarized arms would then intersect at the corotation radius, located at about $r \simeq 2.6$ arcmin (Elmegreen et al. 1992), or 5 kpc. Such an intersection should also occur for the parametric resonance mechanism discussed by Mestel & Subramanian (1991) and Subramanian & Mestel (1993) if the dynamo is assumed to be enhanced in the arms. However, a straightforward modification of this idea assuming that the dynamo action is suppressed in the material arms (Shukurov 1998; Shukurov & Sokoloff 1998; Rohde et al. 1999) can produce interlaced material and magnetic arms near the corotation (Moss 1998).

The theory of slow MHD waves by Fan & Lou (1997) and Lou & Fan (1998) predicts that magnetic arms shifted with respect to the density waves should be present in a rigidly rotating part of the galaxy. However, the rotation of NGC 6946 (as well as of most other galaxies) can hardly be approximated by solid-body rotation. Furthermore, the magnetic arms in NGC 6946 extend out to $r = 11$–12 kpc, that is significantly farther than any rigid-body rotation might be even suspected. In addition, the relative amplitudes of the magnetic and optical arms differently change with radius in the inner part of the galaxy (see Fig. 7).

Sofue (1996) presented a rotation curve for NGC 6946 based on CO and H I data which indicates that strong differential rotation already sets in at about 2-kpc radius. Strong differential rotation would lead to a strong $\alpha\Omega$-dynamo, consistent with the observed strong polarized emission in the inner region of NGC 6946 (Rohde et al. 1999).

The magnetic arms could be due to enhanced dynamo action in the interarm regions or due to suppressed dynamo action in the optical spiral arms (Nozakura 1993; Shukurov 1998; Shukurov & Sokoloff 1998). Moss (1998), Shukurov (1998) and Rohde et al. (1999) predict that the maximum regular magnetic field is located between the material arms around the corotation radius in agreement with the results from this paper. Dynamo models are flexible enough to explain the interlaced material and magnetic arms. The models are sensitive to the spatial distribution of such turbulence parameters as velocity, scale and correlation time. However, very little is known from either observations or modelling about the arm–interarm variation in these parameters. Further progress requires better understanding of the effects of spiral arms on interstellar turbulence. Especially important are the arm–interarm variations in the turbulent velocity (which can be deduced from, say, H I or CO line widths), in the disc scale height and the turbulent scale. Observational estimation of these parameters would require sophisticated statistical analysis of the gas observations. On the other hand, the analysis of this paper can be developed further by using anisotropic wavelets to improve estimates of arm widths and positions, especially in regions where the arms have small pitch angles.

ACKNOWLEDGMENTS

We are grateful to the anonymous referee for useful comments. Financial support from grants RFBR–DFG 96-02-00094G, PPARC GR/L30268, NATO CRG1530959, DFG Eh 154/1-1 and the Royal Society is acknowledged. Fig. 1(e) is based on photographic data of the National Geographic Society – Palomar Observatory Sky Survey (NGS–POSS) obtained using the Oschin Telescope on Palomar Mountain. The NGS–POSS was funded by a grant from the National Geographic Society to the California Institute of Technology. The plates were processed into the present compressed digital form with their permission. The Digitized Sky Survey was produced at the Space Telescope Science Institute under US Government grant NAG W–2166.

REFERENCES

Beck R., Hoernes P., 1996, Nat, 379, 47
Beck R., Brandenburg A., Moss D., Shukurov A., Sokoloff D., 1996, ARA&A, 34, 155
Berkhuijsen E. M., Bajaja E., Beck R., 1993, A&A, 279, 359
Boulanger F., Viallefond F., 1992, A&A, 266, 37
Clausset F., Casoli F., Viallefond F., Combes F., 1991, in Combes F., Casoli F., eds, Dynamics of Galaxies and Their Molecular Cloud Distributions. Kluwer, Dordrecht, p. 88
Ehle M., Beck R., 1993, A&A, 273, 45
Elmegreen D. M., Elmegreen B. G., 1984, ApJS, 54, 127
Elmegreen B. G., Elmegreen D. M., Montenegro L., 1992, ApJS, 79, 37
Fan Z., Lou Y. Q., 1997, MNRAS, 291, 91

Farge M., 1992, Ann. Rev. Fluid Mech., 24, 395
Ferguson A. M. N., Wyse R. F. G., Gallagher J. S., Hunter D. A., 1998, ApJ, 506, L19
Han J., Beck R., Ehle M., Haynes R., Wielebinski R., 1999, A&A, 348, 405
Harnett J. I., Beck R., Buczilowski U. R., 1989, A&A, 208, 32
Holschneider M., 1995, Wavelets: An Analysis Tool. Oxford University Press, Oxford
Kamphuis J., Sancisi R., 1993, A&A, 273, L31
Kennicutt R. C., 1981, AJ, 86, 1847
Krause M., Hummel E., Beck R., 1989, A&A, 217, 4
Lou Y. Q., Fan Z., 1998, ApJ, 493, 102
Mestel L., Subramanian K., 1991, MNRAS, 248, 677
Moss D., 1998, MNRAS, 297, 860
Nozakura T., 1993, MNRAS, 260, 861
Puerari I., Dottori H. A., 1992, A&AS, 93, 469
Roberts W. W., Yuan C., 1970, ApJ, 161, 887
Rohde R., Beck R., Elstner D., 1999, A&A, 350, 423
Sauty S., Gerin M., Casoli F., 1998, A&A, 339, 19
Schlosser W., Musculus D., 1984, A&A, 131, 367
Shukurov A., 1998, MNRAS, 299, L21
Shukurov A., Sokoloff D., 1998, Stud. Geophys. Geod., 42, 391
Sofue Y., 1996, ApJ, 458, 120
Subramanian K., Mestel L., 1993, MNRAS, 265, 649
Sukumar S., Allen R. J., 1989, Nat, 340, 537
Tacconi L. J., Young J. S., 1989, ApJS, 71, 455

This paper has been typeset from a TEX/LATEX file prepared by the author.